Measurement 190 (2022) 110679

Contents lists available at ScienceDirect

Measurement

journal homepage: www.elsevier.com/locate/measurement

In-situ 3D reconstruction of worn surface topography via optimized photometric stereo

Qinghua Wang [a], Shuo Wang [a], Bo Li [a], Ke Zhu [a], Tonghai Wu [a,b,*]

[a] Key Laboratory of Education Ministry for Modern Design and Rotor-Bearing System, Xi'an Jiaotong University, Xi'an, Shaanxi 710049, PR China
[b] Xi'an Jinghui Information Technology Co., Ltd, PR China

A R T I C L E I N F O

Keywords:
Worn surface topography
Photometric stereo
Fused convolutional neural network
Regularized surface reconstruction

A B S T R A C T

Since worn surfaces contain rich information of the wear mechanisms, in-situ measurements of surface topography can characterize ongoing wear degradation in machines. With the help of photometric stereo vision, three-dimensional (3D) topography of worn surfaces is obtained with a monocular microscope. However, the accuracy of the reconstructed surfaces remains low due to the non-Lambertian reflections of worn surfaces and noise in the image acquisition equipment. To address this issue, an optimized photometric stereo approach is proposed for the improvement of worn surface reconstruction. To accommodate the non-Lambertian reflections, a multi-branch network is constructed to estimate normal vectors from both the photometric images and the incident illumination directions. The estimated normal vectors are adopted to reconstruct worn surface topography by embedding prior knowledge. With this design, the overall distortion caused by image noise is effectively suppressed. The proposed method is verified by comparing with the Laser Scanning Confocal Microscopy (LSCM). As the main result, over 88% similarity on the worn surface roughness can be obtained.

1. Introduction

As the direct product of the wear process, worn surfaces with topography variations can indicate the wear evolution [1,2]. Therefore, worn surface analysis is considered an effective means for the state assessment of critical tribological systems [3]. Driven by condition-based maintenance (CBM), this promising technology is developed toward in-situ analysis to provide a comprehensive description for wear condition. However, existing 2D measurements cannot identify topography with similar contours, such as bulges and pits [4,5]. Stereo reconstruction hence has been adopted as a promising method of obtaining 3D topography. Nevertheless, the accuracy is limited by the non-Lambertian reflections and the image noise [6]. Thus, the method for the in-situ acquirement of 3D topography is a challenge for worn surface examination.

Relying on the optical microscope, researchers initially acquire 2D images of worn surfaces to extract characteristics such as invariant moment [7,8]. However, due to the lack of information on the height/depth of the scratches, the 2D image can only characterize surface contours rather than the inner texture for typical surface topography, including bulges and pits. For this reason, 3D scanning devices, for example, Laser Scanning Confocal Microscopy (LSCM) and Atomic Force Microscopy (AFM), have been applied to reconstruct worn surface topography [9]. These devices can provide more morphological features to enhance wear characterization, but they are restricted to laboratory operations. The industrial endoscope [10] can also be adopted to characterize worn surfaces, but only 2D images are provided to realize in-situ examination. With the development of stereo systems, photometric stereo vision [11,12] has been proved to be an effective reconstruction approach for in-situ wear analysis [13–14]. It obtains the surface normal vectors based on the Lambertian reflectance and optimally reconstructs the 3D topography. However, worn surface images are vulnerable to non-Lambertian reflections and image noise, which will result in incorrect normal vector determination and surface reconstruction [15].

Numerous algorithms have been developed for the reconstruction of photometric stereo. To accommodate the non-Lambertian reflections, normal vectors are estimated by outlier rejection or complex reflectance models [16,17]. These estimation algorithms need to calculate the normal vectors pixel by pixel and require many photometric images. With the introduction of neural networks [18–21], the whole normal vector map can be rapidly obtained from photometric images. However, the normal vector estimation accuracy is still affected by the high

* Corresponding author.
E-mail address: wt-h@163.com (T. Wu).

https://doi.org/10.1016/j.measurement.2021.110679
Received 21 May 2021; Received in revised form 30 July 2021; Accepted 29 December 2021
Available online 10 January 2022

reflectivity and multiple reflections in worn surfaces. Moreover, gradient-based reconstruction algorithms, such as the Frankot-Chellappa algorithm [22] and the Poisson algorithm [23], can reconstruct 3D topography from estimated normal vectors. These algorithms assume that the gradient noise satisfies the Gaussian distribution. However, this assumption may not be justified for real-world gradient noise. When the gradient noise accumulates, it further aggravates the distortion of reconstructed surfaces. In contrast to the classical two-step framework, a great likelihood estimate is employed to calculate the height directly from the photometric image [24]. The algorithm enables accurate reconstruction from noisy images, but it is only applicable to Lambertian surfaces due to the assumption of perfect diffuser.

In this work, an optimized photometric stereo approach is developed to reconstruct worn surface topography. Specifically, photometric images of worn surfaces are first collected by an in-situ imaging system. Afterward, a multi-branch network is constructed to estimate normal vectors from the photometric images. The estimated normal vectors and prior knowledge are combined to reconstruct the worn surface topography. The proposed approach is validated with worn surfaces and compared with the standard methods.

The rest of this paper is organized as follows: Section 2 describes the optimized photometric stereo algorithm and its implementation details. The verification of the proposed approach is given in Section 3, followed by the discussion in Section 4. Conclusions are given in Section 5.

2. Materials and methods

2.1. 3D reconstruction of photometric stereo

Focusing on the reconstruction distortion in photometric stereo, the reconstruction process is analyzed to reveal the source of errors. Furthermore, a two-step optimized algorithm is proposed, including the normal vector estimation network (NE-Net) and the regularized surface reconstruction.

2.1.1. Acquisition of photometric images

Fig. 1 depicts the in-situ imaging system adopted to collect photometric images of worn surfaces. In the system, the illumination source consists of eight LEDs circumferentially distributed and independently controlled. The resolution of the digital microscope is 600 pixel × 600 pixel, and the imaging area is 0.732 mm × 0.732 mm. The universal holder and the sliding table are adjusted to ensure clear imaging in the digital microscope. By switching on/off the illumination sources sequentially, eight photometric images are acquired with different illumination directions. These 2D images compose a sample set for 3D image reconstruction of worn surfaces.

2.1.2. Influences of the 3D image reconstruction

Fundamentally, there are two dominant influences to the imaging process: the reflectance properties of worn surfaces and the image noise. They affect the image brightness and introduce errors in the reconstruction process.

The reflectance property, which is critical to the calculation of normal vectors, relates the image brightness to the surface geometry. In conventional photometric stereo algorithms [11], the surface is assumed to be a Lambertian surface containing only diffuse reflections. However, worn surfaces produce various non-Lambertian reflections such as attached shadow, cast shadow, and specular, see Fig. 2. These reflections dramatically change the local brightness and lead to errors in estimating the normal vector.

Image noise originated from the vision sensor will exacerbate surface reconstruction errors. To independently analyze the image noise, noisy Lambertian images are employed to reconstruct 3D topography. These images are rendered from the worn surface topography shown in Fig. 3 (a) and added with Gaussian noise [16] to simulate the real image. Fig. 3 (b-d) show reconstructed surfaces by other reconstruction algorithms, such as the Frankot-Chellappa algorithm [22], the Poisson algorithm [23], and the path-integral algorithm [11]. As can be observed, the reconstructed surfaces contain overall warpage, indicating the accumulation of image noise.

2.1.3. Approach for 3D reconstruction

For the above two influencing factors, a two-step approach is proposed for 3D reconstruction of worn surface topography, see Fig. 4. In the first step, the NE-Net is constructed to estimate a normal vector map

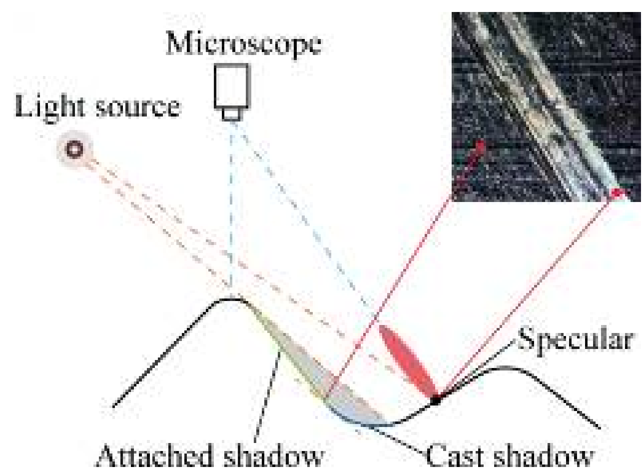

Fig. 2. Reflective components of real worn surfaces.

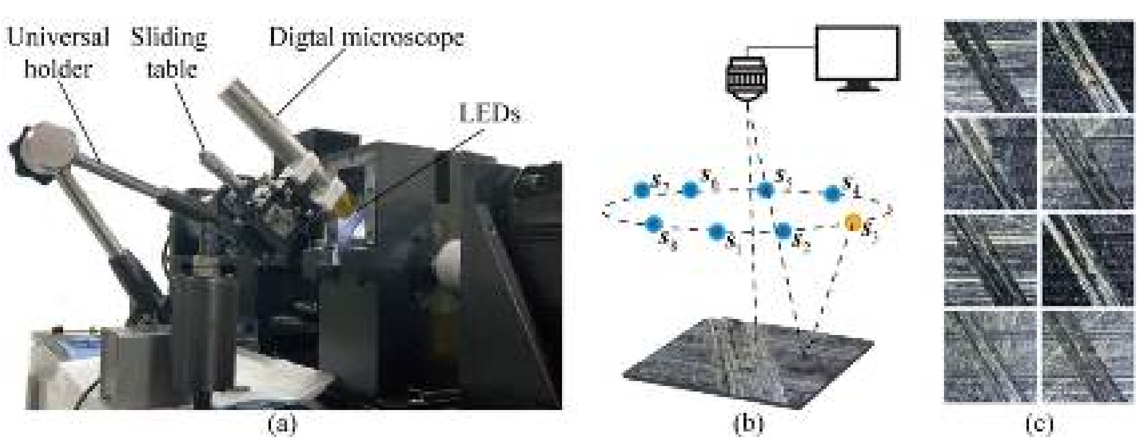

Fig. 1. The in-situ imaging system of worn surfaces (a) system components, (b) illumination source, (c) photometric images.

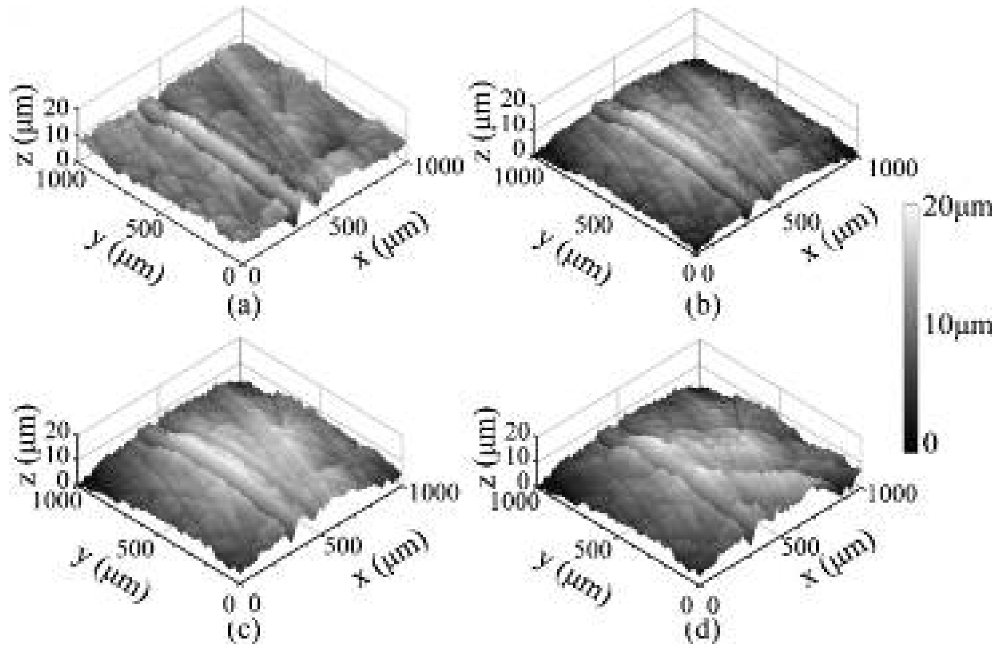

Fig. 3. Reconstructed surfaces with different algorithms (a) ground truth, (b) the Frankot-Chellappa algorithm, (c) the Poisson algorithm, (d) the path-integral algorithm.

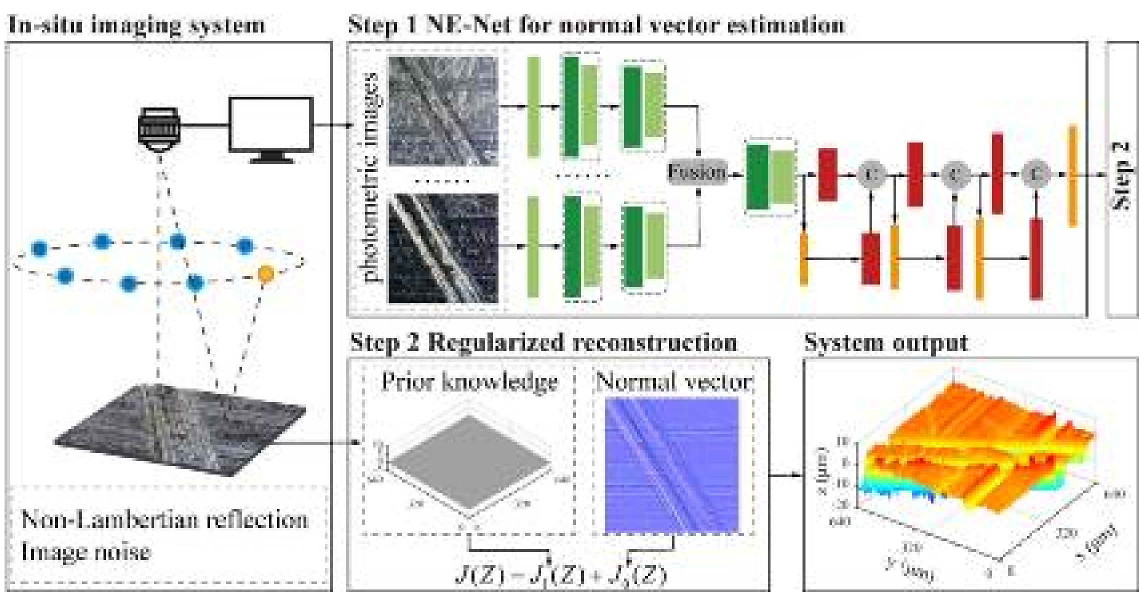

Fig. 4. The framework of the optimization algorithm for 3D reconstruction.

from photometric images of worn surfaces. This is followed by a regularized surface reconstruction step that combines normal vectors and prior knowledge to reconstruct worn surfaces. With the optimization of the normal vector estimation and surface reconstruction, the proposed approach can improve the accuracy. Further details will be introduced in the following sections.

2.2. NE-Net for normal vector estimation

As mentioned before, worn surfaces cannot be regarded as Lambert reflectors due to the appearance of shadows and highlights. For non-Lambertian surfaces, neural networks [18–21] are adopted to establish the relationship between photometric images and normal vector maps. However, the networks with general structures cannot provide the needed accuracy in worn surface reconstruction. To obtain accurate normal vectors, the estimation network is constructed with the combination of the photometric stereo principle.

2.2.1. Structure of NE-Net

As shown in Fig. 5, the NE-Net is a multi-branch network that can output a normal vector map N from photometric images $\boldsymbol{I} = [\boldsymbol{I}_1 \quad \boldsymbol{I}_2 \quad \cdots \quad \boldsymbol{I}_m]$. It is a convolutional network including three components: feature extractor, PS-Fusion, and normal vector generator. The fully convolutional structure is applicable to photometric images of arbitrary size. In the forward propagation, the image size is halved after each convolution layer with a stride of 2 and doubled after a deconvolution layer. For each level, the number of channels is marked below the corresponding layer in Fig. 5. The detailed structure is described below.

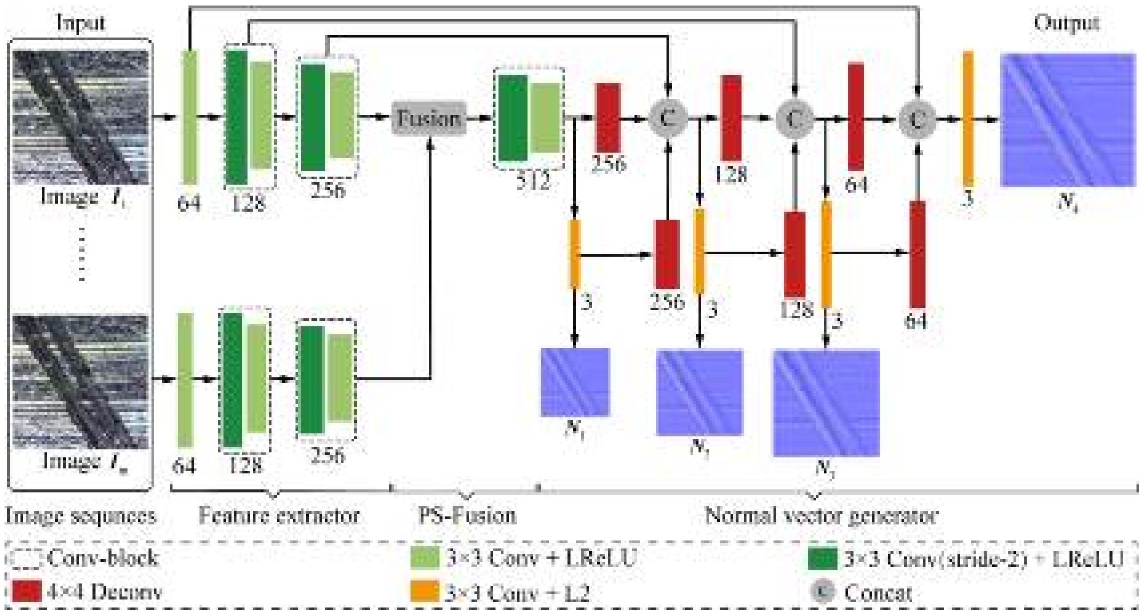

Fig. 5. The structure of the constructed NE-Net.

1) Feature extractor

The feature extractor is designed to excavate beneficial brightness variation from various reflections in photometric images. Specifically, the extractor adopts a multi-branch structure with shared weights to generate independent feature maps. For each branch, a convolutional layer with outside padding converts a photometric image into a feature map with the same resolution. Meanwhile, the conv-block, including two convolutional layers, is employed to process feature maps with resolution compression and channel increment. This structure enables to increase the receptive field and extract high-level information with fewer network parameters. Moreover, the Leaky-ReLu (LReLu) function is added behind each convolutional layer to enhance the non-linearity.

2) PS-Fusion

The extracted feature maps are further aggregated into strong cues for normal vector estimation by the fusion layer. Based on the property of specular reflection, the PS-FCN [18] adopts max-pooling to construct the fused normal vector map. However, the few LED sources can not

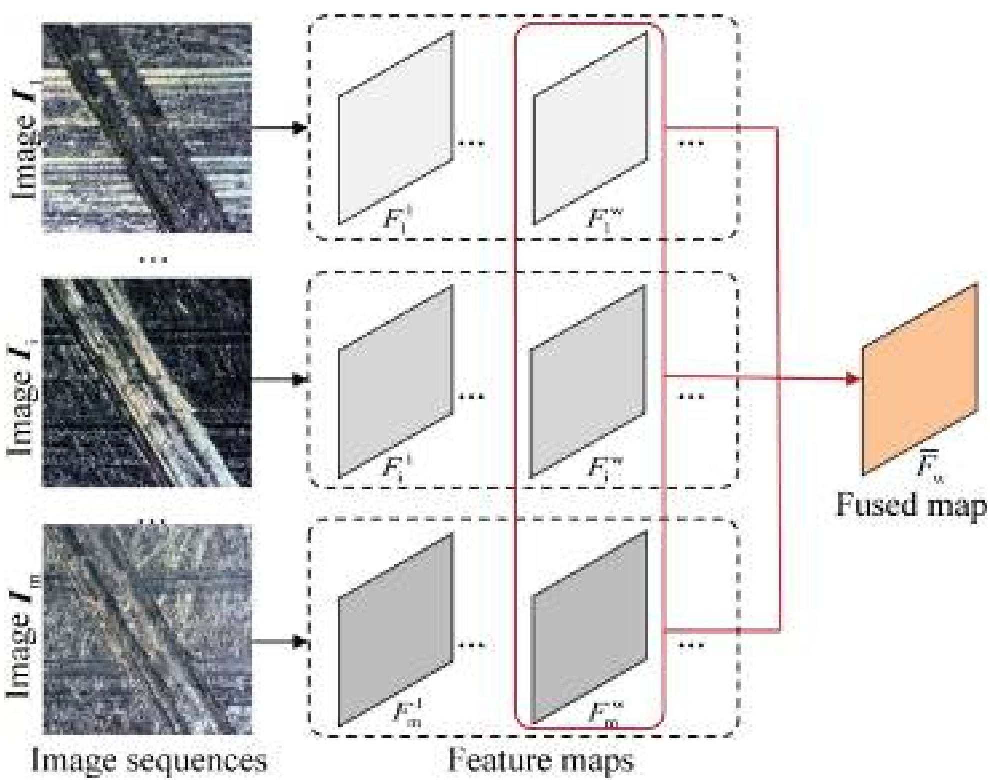

Fig. 6. The schematic of PS-Fusion.

ensure that each pixel exhibits specular reflection from appropriate illumination directions.

To reasonably aggregate feature maps, a photometric stereo fusion (PS-Fusion) method is constructed and is shown in Fig. 6. The design motivation is that the fundamental photometric stereo principle can facilitate NE-Net learning. Specifically, the feature maps at the corresponding channels are treated as a set of photometric images. Based on Lambertian photometric stereo [11], these images are converted to normal vectors as fused feature maps, that is,

$$\overline{F}_w = [\ vec(F_1^w),\quad \cdots,\quad vec(F_i^w),\quad \cdots,\quad vec(F_m^w)\ ]\cdot \boldsymbol{L}^T(\boldsymbol{L}\boldsymbol{L}^T)^{-1} \tag{1}$$

where $\overline{F}_w$ is the w - th fused feature map, F_i^w is the w - th channel of the feature map extracted from image $\boldsymbol{I}_i$, $vec(\cdot)$ represents the vectorization of several matrices, $\boldsymbol{L}$ is the illumination direction matrix consisting of the incident illumination vectors, expressed as $\boldsymbol{L} = [l_1 \quad l_2 \quad \cdots \quad l_m]^T \in \mathbb{R}^{3\times m}$, and the incident illumination vector l_i represents the unit vector directed from the reconstructed surface to the i - th illumination source.

The constructed PS-Fusion can be regarded as an effective extension of the Lambertian photometric stereo algorithm. Compared with max-pooling [26] and mean-pooling [27], this method can reasonably utilize the brightness variations and illumination directions rather than a particular brightness. This design enables high precision normal vector estimation from a few photometric images.

3) Normal vector generator

The normal vector generator is applied to convert fused feature maps into the final normal vector map through the convolutional and deconvolutional layers. To enhance the detail features, normal vector predictions with different resolutions are employed to refine the normal vector map layer by layer. Moreover, the outputs of deconvolutional layers are concatenated with the feature maps from the extractor along the channel dimension. The skip connections can integrate local information from the feature extractor and high-level information supplied by the normal vector generator. Based on the above structure, a dense normal vector map from photometric images is produced from the NE-Net.

2.2.2. Loss function

A proper loss function is essential for the NE-Net to produce accurate normal vector estimation. For each estimated normal vector map, the estimation error is quantified by the cosine similarity (CSIM) loss function. Furthermore, CSIMs of multiple estimations are weighted to form the overall loss function, as shown in Eq. (2). To reinforce the local features, item-by-item doubling weights are employed to focus more on higher feature maps. With the summation of weights close to 1, the four weights are set to 0.08, 0.16, 0.32, and 0.64.

$$\ell_{normal} = \sum_{n=1}^{4} \lambda_n \left(\frac{1}{h_n w_n} \sum_{i=1}^{h_n} \sum_{j=1}^{w_n} (1 - \boldsymbol{N}_{ij} \cdot \widetilde{\boldsymbol{N}}_{ij}) \right) \tag{2}$$

where λ_n is the weight of the n - th normal vector estimation, $h_n \times w_n$ is the resolution of the n - th normal vector map,N_{ij} is the ground truth of the normal vectors at the point (i,j), and $\widetilde{N}_{ij}$ is the estimated value of the normal vector at the point (i,j).

2.2.3. Training of the NE-Net

The essence of NE-Net training is a parameter adjustment process by referring to labeled data containing photometric images and normal vector maps. However, the acquisition of normal vector maps is tedious because it includes 3D measurement, normal vector calculation, and image alignment. These time-consuming operations would lead to difficulties in building a large training set. A simulated worn surface data set is hence used in the NE-Net training.

The build of the simulation dataset is a two-step process: topography simulation and image rendering. In the first instance, topography simulation is performed to generate surface topography consistent with worn surfaces. For worn surfaces, the height obeys Gaussian distribution, and the autocorrelation functions (ACF) satisfy the exponential form [27,28]. Therefore, Gaussian random sequences are employed to generate random surfaces of exponential ACF by 2D digital filtering [29]. Height amplitude and spatial correlation of the generated topography are determined by the RMS roughness and correlation distances. These parameters are consistent with the measurements of worn surfaces to generate realistic topography. This is followed by data-driven rendering to output photometric images from the generated topography. The rendering is implemented based on the MERL database [30], consisting of reflectance data with 100 actual materials. In the generation of simulation data, the RMS roughness is varied, and the correlation distances in different directions are combined to generate diverse topography. Meanwhile, reflectance data with multiple materials are employed to provide distinct reflective properties for simulated surfaces. In this manner, a total of 60,000 sets of simulated data are generated. An example set of simulated data, including a random surface, a normal vector map, and photometric images, are shown in Fig. 7.

With the simulated data, NE-Net parameters are adjusted by minimizing the loss function. The parameter adjustment is implemented using Pytorch 1.9.0. In the training process, the Adam algorithm [31] with default parameters is chosen as the trainer. To eliminate the fluctuation near the optimum point, the learning rate is initially set to 0.001 and divided by two for every five epochs. Moreover, the NE-Net is trained for 30 epochs with a batch size of 32. Fig. 8 depicts the loss function values during the training. It indicates that the NE-Net can estimate normal vectors from simulated images.

2.2.4. Analysis of the NE-Net

The constructed NE-Net is employed to estimate normal vectors in non-Lambertian surfaces. To analyze the effectiveness, a test dataset containing 200 sets of simulated surfaces is built based on the MERL database [29]. Moreover, the analysis adopts the mean angular error (MAE) to quantify the estimation errors.

1) Effectiveness of PS-Fusion

The NE-Net adopts PS-Fusion to fuse multi-branch feature maps in an interpretable way. With the test dataset, the PS-Fusion is compared with max-pooling [25] and mean-pooling [26]. The comparison is with identical remaining layers, and the results are shown in Table 1. It indicates that the constructed PS-Fusion can greatly improve the estimation accuracy.

2) Generalization ability in different materials

Different materials of worn surfaces exhibit distinct reflectance properties, which result in a great challenge for normal vector estimation. To evaluate the performance in different materials, the NE-Net is compared with the Least Squares algorithm (LS) [11] and the Near-field Point Source algorithm (NPS) [14]. The results of comparing 100 materials are shown in Fig. 9. It demonstrates the excellent generalization ability of NE-Net in materials with different reflectance properties. The above two analyses have proved that the NE-Net can produce high-precision normal vector estimation for non-Lambertian surfaces.

2.3. Regularized surface reconstruction from the normal vector map

In addition to non-Lambert reflections, image noise in the image acquisition equipment would aggravate reconstruction distortion. Specifically, accumulated image noise introduces warpage in the reconstructed surfaces, as shown in Fig. 3. To resist the deformation, the prior knowledge of worn surfaces is introduced.

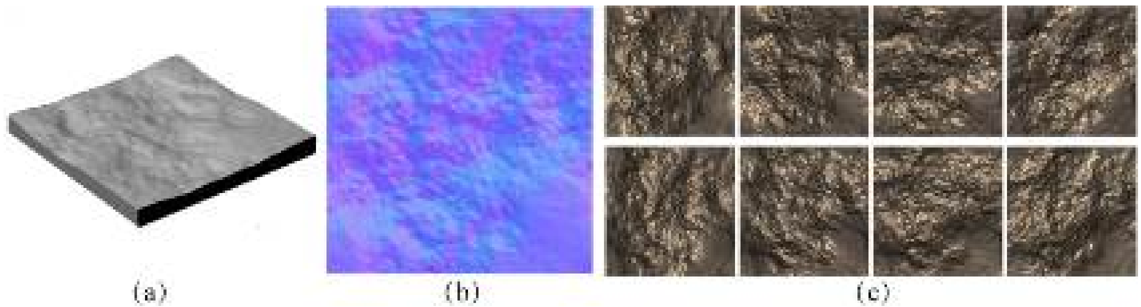

Fig. 7. A set of simulated data: (a) random surface, (b) normal vector map, (c) photometric images.

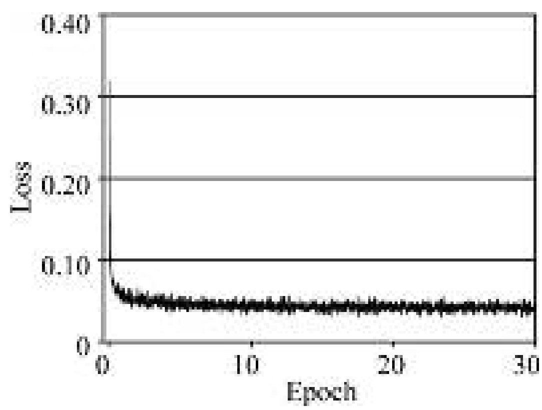

Fig. 8. The training process of the NE-Net.

Table 1
Quantitative comparison of different fusion layers.

Fusion method	Mean-pooling	Max-pooling	PS-Fusion
MAE (°)	7.890	7.021	3.965

2.3.1. *Cost function with prior knowledge*

In photometric stereo, gradient-based reconstruction can recover the 3D topography from the estimated normal vector map. In the first step, estimated normal vectors are converted into gradients based on the perspective projection. This is followed by a cost function [33] described in Eq. (3) to select the surface that satisfies the measured gradients.

$$J_0(Z) = \iint_{(x,y)\in\Omega} [(Z_x(x,y) - p(x,y))^2 + (Z_y(x,y) - q(x,y))^2]dxdy \tag{3}$$

where $Z(x,y)$ is the reconstructed height at the pixel point (x,y), Ω is the reconstructed area, $Z_x(x,y)$ and $Z_y(x,y)$ are the partial derivatives of the reconstructed height, $p(x,y)$ and $q(x,y)$ are the measured gradients.

However, these surfaces exhibit warpages that deviate from the macroscopic appearance. To improve the quality of reconstructed surfaces, the known appearance is embedded in the surface reconstruction as prior knowledge. For example, a flat surface for the pin-on-disc and a cylindrical surface for the bearing outer ring. Specifically, a regularization term containing reconstructed surfaces and prior knowledge is added, the cost function in Eq. (3) becomes:

$$\begin{aligned} J(Z) &= J_0(Z) + J_1(Z) \\ &= \iint_{(x,y)\in\Omega} [(Z_x(x,y) - p(x,y))^2 + (Z_y(x,y) - q(x,y))^2]dxdy \\ &\quad + \iint_{(x,y)\in\Omega} \lambda(Z(x,y) - Z_0(x,y))^2 dxdy \end{aligned} \tag{4}$$

where λ is the regularization coefficient determined by the U-curve [32], Z_0 is the prior knowledge of worn surfaces.

In the constructed cost function, the data term $J_0(Z)$ is employed to reconstruct local features satisfying measured gradients. Moreover, the regularization term $J_1(Z)$ adopts the prior knowledge to suppress image noise accumulation. By balancing both terms, accurate surface topography can be obtained from measured normal vectors.

2.3.2. *Cost function solution for surface reconstruction*

The new cost function describes the difference between reconstructed and real surfaces from the gradients and the prior knowledge. It means that the satisfied surface is selected with the minimum of the cost function. The detailed minimization solution is described as follows.

By transforming numerical differentiation into a matrix multiplication, the partial derivatives of surface height, as $\mathbf{Z}_x$ and $\mathbf{Z}_y$, can be expressed as:

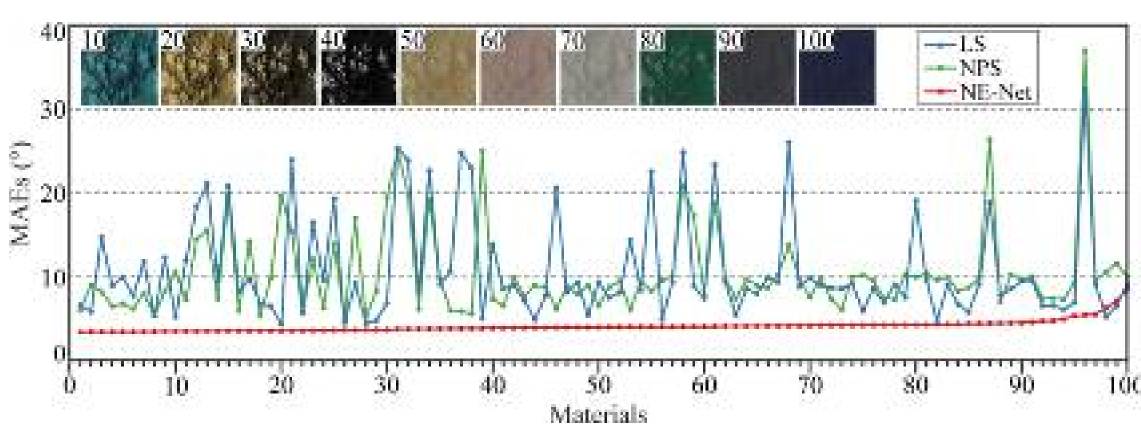

Fig. 9. Quantitative comparison of normal vector estimation algorithms in different materials.

$$\begin{cases} Z_x = ZD_x^T \\ Z_y = D_y Z \end{cases} \tag{5}$$

where Z is the height matrix of the reconstructed surface, D_x and D_y are coefficient matrices of the numerical differentiation.

Based on Eq. (5), the constructed cost function $J(Z)$ is transformed as follows:

$$J(Z) = \text{trace}\{(ZD_x^T - P)(ZD_x^T - P)^T\} + \text{trace}\{(D_yZ - Q)(D_yZ - Q)^T\} \\ +\text{trace}\{\lambda(Z - Z_0)(Z - Z_0)^T\} \tag{6}$$

where P and Q are gradient matrices converted from estimated normal vectors.

To minimize the cost function, Eq. (6) is differentiated with respect to Z, then we have,

$$(D_y^TD_y + \frac{\lambda}{2}I)Z + Z(D_x^TD_x + \frac{\lambda}{2}I) - PD_x - D_y^TQ - \lambda Z_0 = 0 \tag{7}$$

Furthermore, the normal equation is transformed into a Sylvester Equation [34],

$$AZ + BZ = C \tag{8}$$

where $A = D_y^TD_y + \frac{\lambda}{2}I$, $B = D_x^TD_x + \frac{\lambda}{2}I$, $C = PD_x + D_y^TQ + \lambda Z_0$.

Due to the non-zero regularization coefficient, A and B have no common eigenvalue. Hence, the normal function can be solved by the Bartels-Stewart algorithm [34]. With the minimization for the loss function, the reconstructed surface Z is obtained from the measured gradients and the prior knowledge.

2.3.3. Analysis of regularized surface reconstruction

The reconstructed surface by regularized method, as shown in Fig. 10, has no overall warpage compared with other algorithms shown in Fig. 3. These comparisons indicate that the regularized surface reconstruction can suppress image noise accumulation. Furthermore, reconstruction deformations are quantitatively compared by using the root mean square error (RMSE). The comparison is carried out in images with varied signal-to-noise ratios (SNR), as shown in Fig. 11. The result reveals that the regularized surface reconstruction maintains excellent performance over different image noise levels.

3. Verification

In this section, the effectiveness of the constructed algorithm is verified by comparative experiments in worn surfaces containing typical characteristics. First, the in-situ imaging system collects photometric images of worn surfaces. Then, normal vectors and surface heigh are calculated to evaluate the constructed surfaces. Furthermore, the verification incorporates the measurements by LSCM as references.

By using real worn surfaces, the constructed NE-Net is compared with the L1-based estimation (L1) [14], the Least Squares estimation (LS) [11], and the sparse Bayesian learning algorithm (SBL) [16]. The comparison results are shown in Fig. 12 and Table 2. As can be observed, the normal vector estimation errors from different algorithms concentrate at the feature edges. Moreover, the comparison of MAEs shows that the NE-Net performed consistently better than L1, LS, and SBL. It indicates that the NE-Net trained by simulated images can realize the normal vector estimation for worn surfaces.

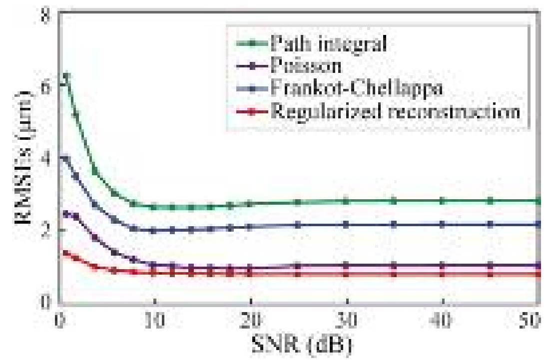

Fig. 11. Quantitative comparison of different reconstruction algorithms.

In addition to the verification of the NE-Net, the entire two-step algorithm is verified with reconstructed surfaces. The verification adopts LSCM and the original reconstruction algorithm [14] as comparisons. Fig. 13 shows the reconstructed surfaces with the three methods. As may be observed, the surfaces reconstructed by the original algorithm exhibit large deformations, such as the deformed bulge and the warpage around scratch. More importantly, the reconstructed surfaces of the proposed algorithm have realized a high similarity with the measurement by LSCM. Hence, it proves that the constructed algorithm can obtain reconstructed surfaces with high accuracy.

The quantitative analysis is performed to further verify the proposed reconstruction approach. Compared to 2D quantization parameters, 3D parameters can characterize the whole worn surface rather than a specific contour or texture. Among 3D parameters, the surface arithmetic mean deviation (Sa) describes the roughness of the worn surface, reflecting the wear severity of the friction pair. Therefore, the Sa is applied to compare the original and proposed reconstruction algorithms quantitatively. As shown in Table 3, the Sa from the original algorithm deviated from the true value, but all Sa errors from the proposed algorithm are less than 12%. The comparison results reveal that the constructed algorithm enables the improvement of worn surface reconstruction.

4. Discussion

The worn surface reconstruction is improved by an optimized photometric stereo algorithm, including two improvements: the NE-Net for normal vector estimation and the regularized surface reconstruction with prior knowledge. The algorithm can effectively handle the non-

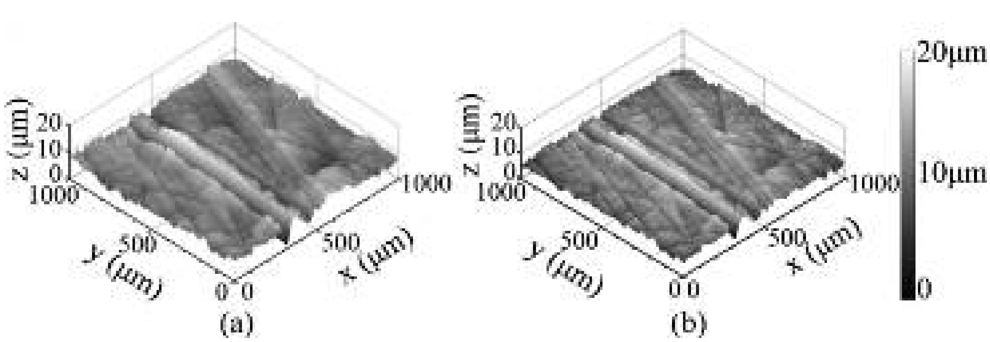

Fig. 10. The regularized surface reconstruction from noisy Lambertian images: (a) ground truth, (b) reconstructed surface.

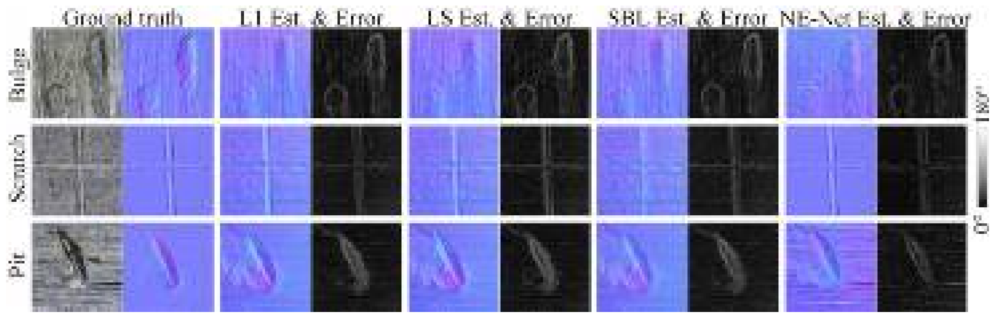

Fig. 12. Estimated normal vector map of real worn surfaces.

Table 2
The MAEs of different algorithms in real worn surfaces (°).

Algorithm	Bulge	Scratch	Pit
L1	22.43	21.34	21.05
LS	22.71	21.88	21.13
SBL	23.41	23.27	22.39
NE-Net	17.28	15.78	17.70

Lambert reflections and image noise, and reduce the reconstruction errors. Compared to conventional measurement methods, the proposed algorithm possesses distinctive advantages described below.

Compared with offline measurement methods [7–9], the proposed method reconstructs worn surfaces based on in-situ image acquisition, which greatly improved the wear analysis efficiency. Although the industrial endoscope [10] is available for in-situ analysis, the obtained images still impose difficulties in characterizing similar features on worn surfaces. Moreover, the existing photometric stereo algorithm [14] is restrictive due to non-Lambertian reflections and image noise in the image acquisition equipment. To improve the accuracy of reconstructed surfaces, the normal vector estimation and gradient-based reconstruction processes are optimized. Therefore, the developed approach is effective for in-situ measurement of worn surfaces.

Although the proposed approach can improve the surface reconstruction accuracy, the measurement resolution and range are still limited by the digital microscope. Moreover, the ultimate purpose of this work is to improve the accuracy and efficiency of wear analysis. Therefore, future work will focus on the wear mechanism research with 3D surface topography. Based on the in-situ measurement, typical surface topography will be collected to construct the worn sample database. Furthermore, wear mechanism identification may be developed with numerous intelligent algorithms.

5. Conclusions

An optimized photometric stereo approach is proposed to improve worn surface reconstruction. The main features are 1) with the

Table 3
The Sa comparison with different reconstruction algorithms.

Worn surface	LSCM (μm)	Original algorithm		Proposed algorithm	
		Value (μm)	Error	Value (μm)	Error
Bulge	5.0864	2.1040	58.63%	4.7410	4.74%
Scratch	0.9842	1.8356	86.51%	1.0703	8.75%
Pit	2.6217	3.2631	24.47%	2.9215	11.44%

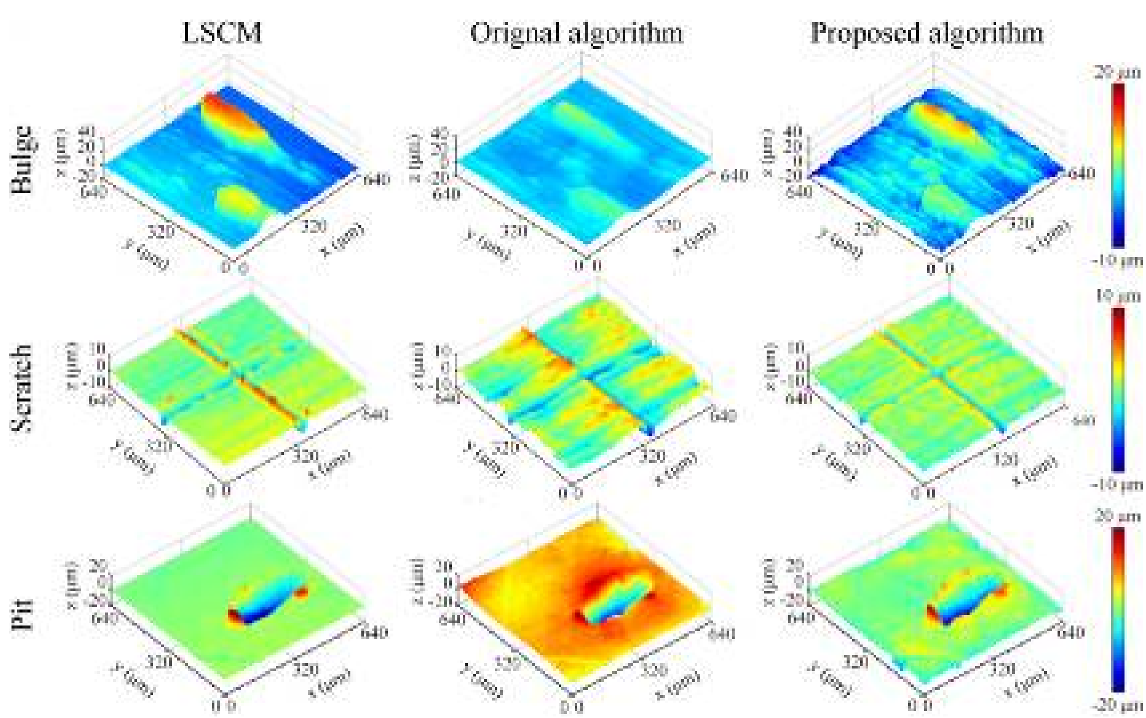

Fig. 13. Reconstruction comparison with different methods.

Table A1
Multiple materials adopted in the quantitative comparison of normal vector estimation algorithms.

No.	Material	No.	Material	No.	Material
1	green-metallic-paint	35	yellow-paint	69	white-acrylic
2	silver-metallic-paint	36	fruitwood-241	70	red-specular-plastic
3	gold-metallic-paint2	37	colonial-maple-223	71	white-diffuse-bball
4	silver-metallic-paint2	38	natural-209	72	maroon-plastic
5	two-layer-silver	39	chrome	73	dark-specular-fabric
6	special-walnut-224	40	red-plastic	74	white-fabric2
7	two-layer-gold	41	dark-blue-paint	75	polyethylene
8	silver-paint	42	teflon	76	specular-white-phenolic
9	blue-metallic-paint	43	yellow-matte-plastic	77	specular-red-phenolic
10	gold-metallic-paint3	44	dark-red-paint	78	green-acrylic
11	gold-metallic-paint	45	yellow-phenolic	79	pink-fabric
12	green-metallic-paint2	46	pvc	80	green-latex
13	blue-metallic-paint2	47	specular-yellow-phenolic	81	white-fabric
14	violet-acrylic	48	pickled-oak-260	82	nylon
15	color-changing-paint1	49	red-fabric	83	white-paint
16	alum-bronze	50	purple-paint	84	aventurnine
17	hematite	51	white-marble	85	green-plastic
18	gold-paint	52	blue-rubber	86	yellow-plastic
19	orange-paint	53	red-phenolic	87	specular-black-phenolic
20	color-changing-paint3	54	alumina-oxide	88	specular-blue-phenolic
21	color-changing-paint2	55	gray-plastic	89	pure-rubber
22	cherry-235	56	delrin	90	green-fabric
23	brass	57	pink-felt	91	pink-plastic
24	brass	58	chrome-steel	92	specular-maroon-phenolic
25	aluminium	59	grease-covered-steel	93	specular-green-phenolic
26	black-soft-plastic	60	specular-orange-phenolic	94	specular-violet-phenolic
27	nickel	61	steel	95	red-fabric2
28	black-oxidized-steel	62	pink-fabric2	96	black-obsidian
29	light-red-paint	63	blue-acrylic	97	blue-fabric
30	red-metallic-paint	64	neoprene-rubber	98	polyurethane-foam
31	black-phenolic	65	violet-rubber	99	light-brown-fabric
32	ss440	66	pink-jasper	100	black-fabric
33	ipswich-pine-221	67	beige-fabric		
34	tungsten-carbide	68	silicon-nitrade		

combination of the photometric stereo principle and the multi-branch network, the NE-Net is constructed to estimate normal vectors from non-Lambertian images; 2) through embedding the prior knowledge of worn surfaces, image noise acclamation is suppressed in reconstructing 3D topography from estimated normal vectors. Compared with the LSCM, the proposed approach obtains highly similar reconstructed surfaces with less than 12% Sa errors. This work provides a 3D characterization for worn surfaces through in-situ measurement, and it will promote the development of wear mechanism analysis.

CRediT authorship contribution statement

Qinghua Wang: Conceptualization, Methodology, Writing – original draft. **Shuo Wang:** Writing – review & editing. **Bo Li:** Investigation. **Ke Zhu:** Software, Validation. **Tonghai Wu:** Supervision.

Declaration of Competing Interest

The authors declare that they have no known competing financial interests or personal relationships that could have appeared to influence the work reported in this paper.

Acknowledgements

The authors appreciate the financial support from the National Key R&D Program of China (Grant No. 2018YFB1306100), the National Natural Science Foundation of China (Nos. 51975455 and 52105159) and the China Postdoctoral Science Foundation (No. 2021M702594).

Appendices

The NE-Net is quantitatively compared with other normal vector estimation algorithms in different materials to evaluate the generalization capability. The adopted materials in the comparison are shown in Table A.1.

References

[1] Z. Liu, L. Zhang, A review of failure modes, condition monitoring and fault diagnosis methods for large-scale wind turbine bearings, Measurement 149 (2020) 107–129, https://doi.org/10.1016/j.measurement.2019.107002.
[2] W.T. Zhu, L.C. Guo, L.B. Shi, Z.B. Cai, Q.L. Li, Q.Y. Liu, W.J. Wang, Wear and damage transitions of two kinds of wheel materials in the rolling-sliding contact, Wear 398 (2018) 79–89, https://doi.org/10.1016/j.wear.2017.11.023.
[3] J.P. Salameh, S. Cauet, E. Etien, A. Sakout, L. Rambault, Gearbox condition monitoring in wind turbines: a review, Mech. Syst. Sig. Process. 111 (2018) 251–264, https://doi.org/10.1016/j.ymssp.2018.03.052.
[4] J. Zhou, Q. Zhou, L. Yang, G. Wu, Acquisition and rendering of characteristic images of the wear surfaces of running parts within machinery, Wear 265 (3-4) (2008) 540–545, https://doi.org/10.1016/j.wear.2007.09.002.
[5] S. Soleimani, J. Sukumaran, A. Kumcu, P. De Baets, W. Philips, Quantifying abrasion and micro-pits in polymer wear using image processing techniques, Wear 319 (1-2) (2014) 123–137, https://doi.org/10.1016/j.wear.2014.07.018.
[6] Y. Tian, J. Wang, Z. Peng, X. Jiang, A new approach to numerical characterisation of wear particle surfaces in three-dimensions for wear study, Wear 282–283 (2012) 59–68, https://doi.org/10.1016/j.wear.2012.02.002.
[7] C. Wang, F. Li, Y. Li, H. Chen, X. Cao, in: A defect status detecting method for external gear in railway, in, IEEE, Chongqing, 2018, pp. 123–127, https://doi.org/10.1109/ICIVC.2018.8492899.
[8] O. Moldovan, S. Dzitac, I. Moga, T. Vesselenyi, I. Dzitac, Tool-wear analysis using image processing of the tool flank, Symmetry. 9 (2017) 296, https://doi.org/10.3390/sym9120296.
[9] Z. Yi, Z. Chen, Z. Jiang, W. Gui, A novel 3-D high-temperature industrial endoscope with large field depth and wide field, IEEE Trans. Instrum. Meas. 69 (9) (2020) 6530–6543, https://doi.org/10.1109/TIM.2020.2970372.
[10] S. Martelli, L. Mazzei, C. Canali, P. Guardiani, S. Giunta, A. Ghiazza, I. Mondino, F. Cannella, V. Murino, A.D. Bue, Deep endoscope: intelligent duct inspection for the avionic industry, IEEE Trans. Ind. Inf. 14 (4) (2018) 1701–1711, https://doi.org/10.1109/TII.2018.2807797.
[11] V. Argyriou, M. Petrou, Chapter 1 photometric stereo: an overview, in: Advances in Imaging and Electron Physics, Elsevier, 2009: pp. 1–54. https://doi.org/10.1016/S1076-5670(08)01401-8.
[12] R.J. Woodham, Photometric method for determining surface orientation from multiple images, Opt. Eng. 19 (1) (1980), 191139, https://doi.org/10.1117/12.7972479.
[13] S. Wang, T. Wu, L. Yang, N. Kwok, T. Sarkodie-Gyan, Three-dimensional reconstruction of wear particle surface based on photometric stereo, Measurement 133 (2019) 350–360, https://doi.org/10.1016/j.measurement.2018.10.032.
[14] C. Xu, T. Wu, Y. Huo, H. Yang, In-situ characterization of three dimensional worn surface under sliding-rolling contact, Wear 426–427 (2019) 1781–1787, https://doi.org/10.1016/j.wear.2018.12.045.
[15] Y. Mukaigawa, Y. Ishii, T. Shakunaga, Analysis of photometric factors based on photometric linearization, J. Opt. Soc. Am. A. 24 (2007) 3326–3334, https://doi.org/10.1364/JOSAA.24.003326.
[16] S. Ikehata, D. Wipf, Y. Matsushita, K. Aizawa, Photometric stereo using sparse bayesian regression for general diffuse durfaces, IEEE Trans. Pattern Anal. Mach. Intell. 36 (2014) 1816–1831, https://doi.org/10.1109/TPAMI.2014.2299798.
[17] H. Santo, M. Samejima, Y. Sugano, B. Shi, Y. Matsushita, Deep photometric stereo Network, in: 2017 IEEE International Conference on Computer Vision Workshops (ICCVW), Venice, 2017: pp. 501–509. https://doi.org/10.1109/ICCVW.2017.66.

[18] G. Chen, K. Han, K.-Y.K. Wong, PS-FCN: a flexible learning framework for photometric stereo, in: European Conference on Computer Vision, Springer International Publishing, Cham, 2018: pp. 3–19. https://doi.org/10.1007/978-3-030-01240-3_1.
[19] B. Shi, Z. Wu, Z. Mo, D. Duan, S.-K. Yeung, P. Tan, A benchmark dataset and evaluation for non-lambertian and uncalibrated photometric stereo, IEEE Conf. Comput. Vis. Pattern Recogn. (2016) 3707–3716.
[20] V. Badrinarayanan, A. Kendall, R. Cipolla, SegNet: a deep convolutional encoder-decoder architecture for image segmentation, IEEE Trans. Pattern Anal. Mach. Intell. 39 (12) (2017) 2481–2495, https://doi.org/10.1109/TPAMI.2016.2644615.
[21] T. Taniai, T. Maehara, Neural photometric stereo reconstruction for general reflectance surfaces, Int. Conf. Mach. Learn. (2018) 4864–4873.
[22] R.T. Frankot, R. Chellappa, A method for enforcing integrability in shape from shading algorithms, IEEE Trans. Pattern Anal. Mach. Intell. 10 (1988) 439–451, https://doi.org/10.1109/34.3909.
[23] T. Simchony, R. Chellappa, M. Shao, Direct analytical methods for solving Poisson equations in computer vision problems, IEEE Trans. Pattern Anal. Mach. Intell. 12 (1990) 435–446, https://doi.org/10.1109/34.55103.
[24] L. Noakes, R. Kozera, Nonlinearities and Noise Reduction in 3-Source Photometric Stereo, J. Math. Imag. Vis. 18 (2003) 119–127, https://doi.org/10.1023/A:1022104332058.
[25] Y. Queau, J.-D. Durou, J.F. Aujol, Normal integration: a survey, J. Math. Imag. Vis. 60 (2018) 576–593. http://arxiv.org/abs/1709.05940.
[26] O. Wiles, A. Zisserman, SilNet : single- and multi-view reconstruction by learning from silhouettes, British Mach. Vis. Conf. (2017). http://arxiv.org/abs/1711.07888.
[27] W. Hartmann, S. Galliani, M. Havlena, L. Van Gool, K. Schindler, Learned multi-patch similarity, in: 2017 IEEE International Conference on Computer Vision (ICCV), IEEE, Venice, 2017: pp. 1595–1603. https://doi.org/10.1109/ICCV.2017.176.
[28] R. Reizer, P. Pawlus, L. Galda, W. Grabon, A. Dzierwa, Modeling of worn surface topography formed in a low wear process, Wear 278–279 (2012) 94–100, https://doi.org/10.1016/j.wear.2011.12.012.
[29] M.W. Chui, Y.Q. Feng, W. Wang, P.L. Li, Z.C. Li, Numerical simulation of rough surface with crossed texture, Appl. Mech. Mater. 321 (2013) 196–200, https://doi.org/10.4028/www.scientific.net/AMM.321-324.196.
[30] W. Matusik, H. Pfister, M. Brand, L. McMillan, A data-driven reflectance model, ACM Trans. Graph. 22 (3) (2003) 759–769, https://doi.org/10.1145/882262.882343.
[31] D.P. Kingma, J. Ba, Adam: a method for stochastic optimization, Computer, Science (2017). http://arxiv.org/abs/1412.6980.
[32] D. Krawczyk-Stańdo, M. Rudnicki, Regularization parameter selection in discrete ill-posed problems — the use of the U-curve, Int. J. Appl. Math. Comput. Sci. 17 (2007) 157–164, https://doi.org/10.2478/v10006-007-0014-3.
[33] M. Harker, P. O'Leary, Regularized reconstruction of a surface from its measured gradient field, J. Math. Imaging Vision 51 (1) (2015) 46–70, https://doi.org/10.1007/s10851-014-0505-4.
[34] G. Golub, S. Nash, C. Van Loan, A hessenberg-schur method for the problem AX + XB= C, IEEE Trans. Autom. Control. 24 (6) (1979) 909–913, https://doi.org/10.1109/TAC.1979.1102170.